Computational laboratories, test case 2

Turbulent water transport in a hydraulically smooth pipeline

Francesco Derme, Pietro Di Giustino, Pietro Fumagalli

1 Introduction

We simulate the turbulent flow of water at 20°C, treated as incompressible in a hydraulically smooth pipeline of diameter $D = 0.1m$, so we have $\rho = 998.23\frac{kg}{m^3}$ and $\nu = 10^{-6}\frac{m^2}{s}$, pipe roughness ≈ 0. If the pipeline is sufficiently long and a uniform velocity profile is imposed at the inlet boundary, one expects the flow to reach the fully developed state at a certain distance downstream of it, this region will be of interest to our analysis. Furthermore, because of the inherently unsteady nature of turbulence, considerations are only made in a time-averaged sense. The quantities of interest are the frictional losses along the pipeline as well as the radial profiles of the axial velocity, of the shear stresses and of the turbulent parameters. Since no analytical solution is available for this setup, experimental data and empirical correlations are used for validation.

The flow is simulated by solving the RANS equations coupled with the standard k-ϵ turbulence model. The wall function approach is adopted to model the effect of near-wall turbulence, and the equilibrium wall function of Launder and Spalding is employed. The computational burden of the simulations can be reduced by exploiting the axisymmetry of the mean flow field, which will be therefore simulated as 2D through a domain having the shape of a circular sector.

The boundary conditions used are inlet, outlet, solid walls, and axis.

- At the inlet, a uniform z-velocity profile of value $W_b = 0.75\frac{m}{S}$ is imposed, whereas the r and θ velocity components are set to zero. No turbulence is assumed at the inlet, this is achieved by setting the turbulence intensity parameter TI to 0.
- At the outlet, a zero external pressure P^* is imposed.
- At the solid walls, owing to the no-slip condition, the fluid velocity is zero. In the Finite Volume framework with staggered-grid arrangement, only the r-velocity is imposed at the wall. The no-slip condition is imposed for the z-velocity indirectly. On the one hand, the advection flux of variable W through the near-wall cell faces is set to zero. On the other hand, the diffusion flux of variable W through the near-wall cell faces, i.e. the wall shear force, is specified by obtaining the wall shear stress from the equilibrium wall function of Launder and Spalding. Note that, since the wall function approach is adopted, the dimensionless wall distance y^+ of the first grid nodes must be greater than 30 and lower than 130. Such dimensionless wall distance can only be calculated a posteriori.

This set of boundary conditions results in a developing flow field which, starting from the uniform distribution imposed at the inlet section, reaches a fully developed configuration at a certain distance downstream of it.

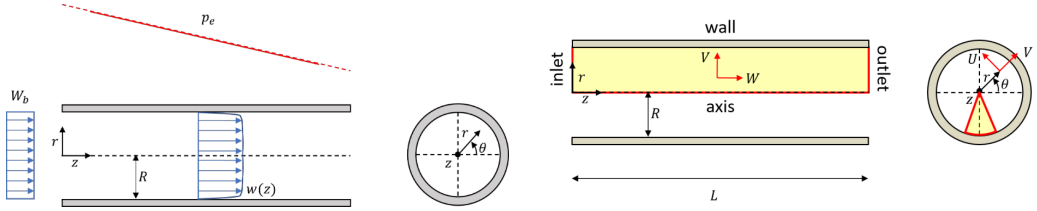

2 Analysis

1. In order to verify that the setting induces a turbulent flow, the Reynolds bulk number Re_b is calculated. The velocity to be used in this computation is the bulk velocity (it would make no sense to use the axial velocity which depends on the specific coordinates, the bulk velocity is instead constant along the length of the pipe as a result of mass conservation). Since Re_b exceeds the threshold value of about 2000, the flow is turbulent.

$$Re_b = \frac{W_b \cdot D}{\nu} = \frac{0.75 \cdot 0.1}{10^{-6}} \approx 75 \ \cdot 10^3 > 2000 \tag{1}$$

2. A certain the domain length L must be chosen to run the simulation in such a way that fully developed flow conditions are attained from the uniform velocity profile imposed at the inlet, this means that the z-derivative of all the Reynolds-averaged variables, except for the pressure, must become 0. The goal is not to determine accurately the length required for flow development, i.e. the entry length L_e, but simply to observe fully developed flow in the CFD solution. In principle, fully developed flow is reached in an asymptotic manner, at an infinite distance downstream of the inlet, so practical criteria need to be developed to assess that the fully developed flow condition has been reached. We set $L = 6m$ and support our choice by inspecting qualitatively the CFD solution, by providing quantitative, although arbitrary, thresholds and finally by a comparison against available formulas.

   Looking closely at the z-velocity profile we observe that the centerline velocity reaches its peak at about 2.6 meters and then it starts decreasing and doesn't actually settle down completely until about 4 meters. This is meaningful because this region, the centerline, is generally where the flow goes the fastest and takes the longest to reach full development. The choice of $L = 6m$ thus leaves us ample space to observe the characteristics of fully developed flow without inducing too much computational overhead.

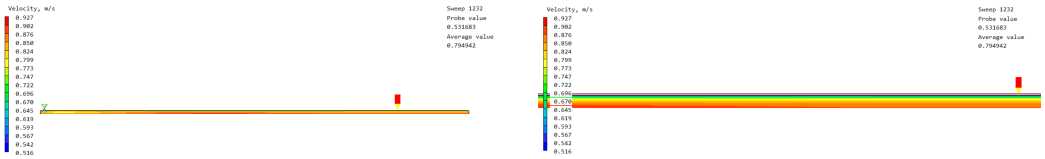

   We compute the incremental ratio of the centerline velocity by subtracting the velocities stored in two adjacent cells and then normalizing it by the length of the distance between the storage points of the two variables, since our simulations always define uniform meshes in the z direction, this distance is constant and equal to the length of a cell. We define our custom entry as the distance from the inlet where the incremental ratio goes below 0.01 **definitively**, indeed it may happen that this quantity decreases under our threshold and then increases again. Of course the choice of the threshold value of 0.01 is arbitrary but this generally leads to a more restrictive criterion with respect to the ones found in literature as we'll discuss below. Using this criterion we find $L_e = 4.26m$. We also try to run the simulation with a shorter pipe length of $3m$ to compare it with our default simulation that stands at $6m$. We plot the centerline velocities and clearly observe that the simulation with shorter pipe length doesn't attain the fully developed state.

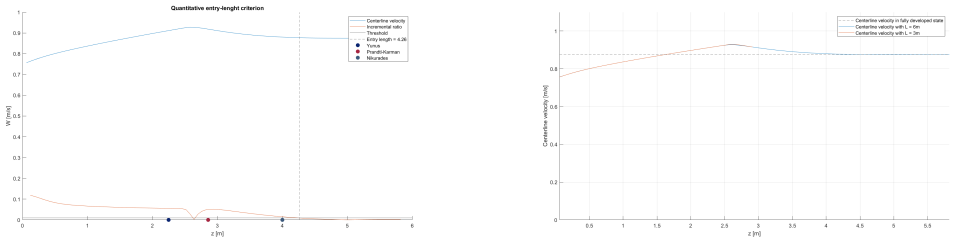

We select some literature metrics for L_e in order to compare them to our custom criterion:

- Yunus: $L_e = (1.359 \cdot Re_b^{\frac{1}{4}}) \cdot D \approx 2.249m$
- Prandtl-Karman: $L_e = 4.4 \cdot Re_b^{\frac{1}{6}} \cdot D \approx 2.8573m$
- Nikurades: $L_e = 40 \cdot D = 4m$
- Lien at. Al: $L_e = 150 \cdot D = 15m$

All these criteria are less restrictive than ours except for the last one, this was presented by Lien at. Al in the Australasian Fluid Mechanics Conference in a paper titled *The Entrance Length for Fully Developed Turbulent Channel Flow*. The authors were referring to Reynolds numbers up to $185 \cdot 10^3$ and so we deem it not applicable to our case.

Finally, we show that the nature of the flow, laminar or turbulent, affects the length required for flow development by comparing literature formulas for the two cases. To this aim we express the entry lengths in dimensionless form, normalizing them with respect to the pipe diameter.

3. The solution is physically, qualitatively sound. The color plots of pressure and velocity don't exhibit any strange pattern, instead the variables behave exactly as expected with the θ and r components of the velocity being null and the axial velocity reaching its maximum in the center of the pipe. The pressure, as we expect, decreases linearly as this is a pressure-driven flow.

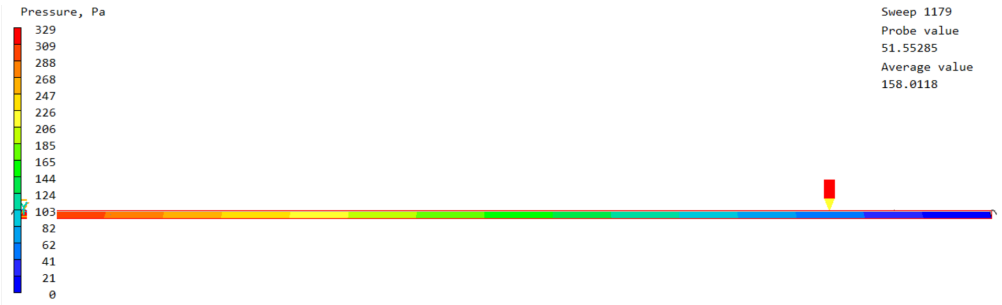

To the aim of demonstrating the physical consistency of our results we plot: the distribution of pressure P^* along the axis of the pipe, the profile of the Reynolds average velocity along the pipe radius in dimensionless form both as $\frac{W}{W_b}$ versus $\frac{r}{R}$ where R is the radius of the pipe and as w^+ versus y^+, where $w^+ = \frac{W}{w_\tau}$ and $y^+ = \frac{y \cdot w_\tau}{\nu}$, being $w_\tau = \sqrt{\frac{\tau_w}{\rho}}$ the friction velocity and $y = R - r$ the distance from the pipe wall, this one will be presented as a log-log plot. The values of y^+ mentioned from here on out are calculated either by referring to the *PHOENICS* variable YPLS which stores the non-dimensional wall distance of the first grid nodes in wall units or directly by the formula above. Furthermore we plot: the profile of the total shear stresses $\tau(r)$ and of its components $\tau_{visc}(r)$ and $\tau_{Re}(r)$ along the pipe radius normalized by τ_w versus r/R, the profile of the turbulent kinetic energy k along the pipe radius, presented in dimensionless form as $\frac{k}{W_b^2}$ versus $\frac{r}{R}$ and finally the profile of the turbulent dissipation rate ϵ along the pipe radius, presented in dimensionless form as $\frac{\epsilon \cdot R}{W_b^3}$ versus $\frac{r}{R}$.

Note that the values of $\tau_{visc}(r)$ and $\tau_{Re}(r)$ are obtained numerically from the constitutive model for the stresses tensor and the Boussinesq assumption of eddy viscosity for the Reynolds stresses tensor, that is, $\tau_{visc}(r) = \mu \frac{dw}{dr}$ and $\tau_{Re}(r) = \mu_t \frac{dw}{dr}$. Conversely, the wall shear stress cannot be evaluated from the axial velocity profile because the wall function approach requires $y^+ > 30$, hence the center of the cell nearest to the wall is already in the log branch of the equilibrium wall function by Launder and Spalding. τ_w is rather derived from the *PHOENICS* output variable STRS $= \frac{\tau_w}{\rho} = w_\tau^2$. We evaluated the parameter μ_t in two different ways: as $rho \cdot C_\mu \cdot \frac{k^2}{\epsilon}$ with a value of 0.09 for C_μ taken from the literature or starting from the *PHOENICS* output variable representing kinematic eddy viscosity ENUT $= \frac{\mu_t}{\rho}$, they proved equivalent as the pseudo L_1 norm of their difference was $1.8723e \cdot 10^{-4}$ and the second method was chosen as it seemed more direct. Please also note that in order to improve the numerical estimate of the shear stresses, we use arithmetic averaging for the diffusion coefficients of the variable W, i.e. the z-velocity.

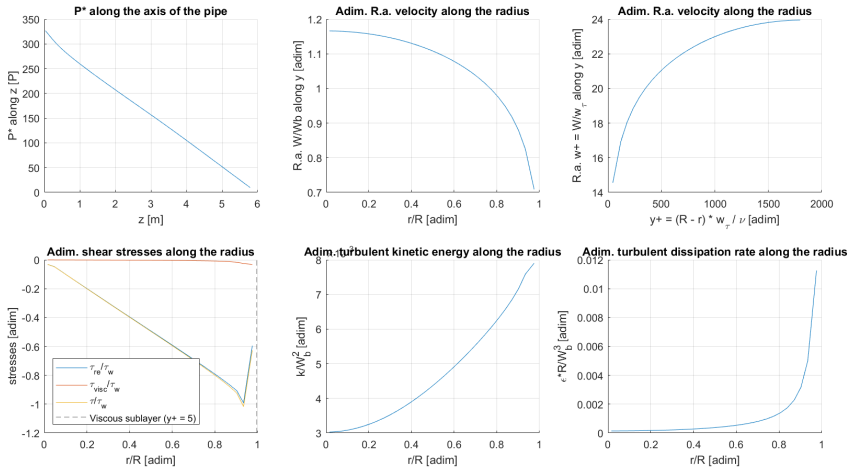

The plots of W show the flat profile that is to be expected in a turbulent case, the velocity does not reach 0 at the wall since $y^+ \approx 40$ in the fully developed region. The trends of the stresses match turbulent flow theory: the viscous component is irrelevant far from the wall and becomes more impactful the closer we get to it, at the same time τ_{Re} starts decreasing and is finally overtaken by τ_{visc} in the viscous sublayer that is plotted but to small to be appreciable.

4. We assess the numerical convergence of the CFD solution by, on the one hand, verifying that the CFD simulation is converged with respect to the solution algorithm and, on the other, that the solution is grid independent. We demonstrate the convergence with respect to the solution algorithm by showing the normalized whole-field residuals, the max corrections, the spot values and the max/min values. The first two tend to 0, or rather they stabilize below the threshold of 10^{-3}, the rest converge to a fixed value, respecting our convergence criteria long before the maximum number of iterations was reached.

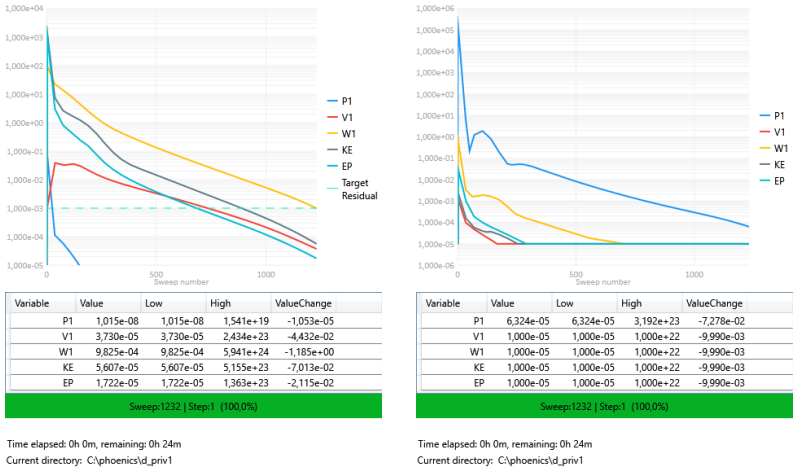

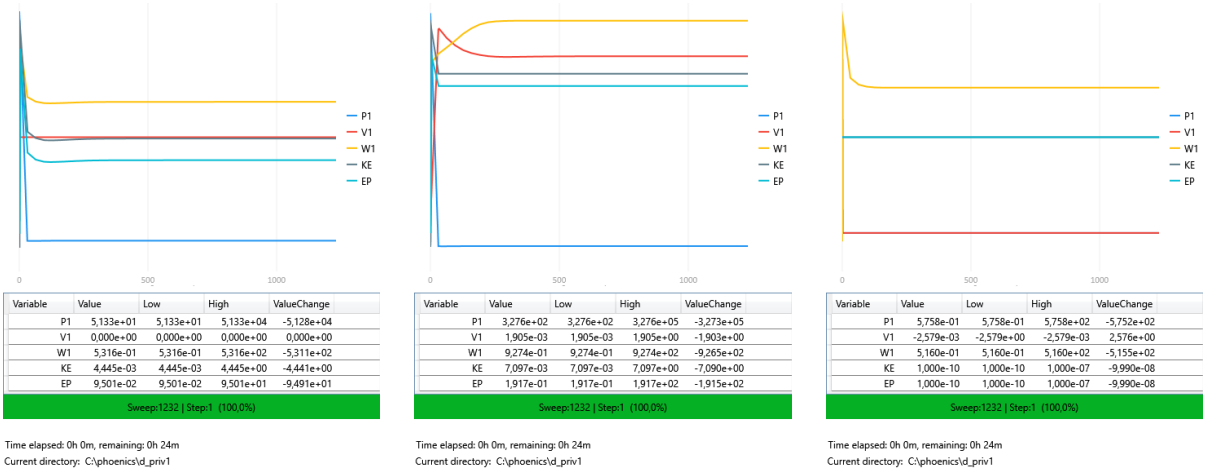

The target parameters of our grid independence study are W, $\frac{dW}{dy}$, P^*, k and ϵ, all of which have been proven grid-independent. We investigated increasing mesh refinement levels along both the z and r directions both separately and jointly. In particular, the chosen meshes are shown in the table below.

Mesh name	# cells along x	# cells along y	# cells along z	Power law
Base case	1	30 + 1	100	No
ref 1	1	60 + 1	100	No
ref 2	1	90 + 1	100	No
ref 3	1	30 + 1	150	No
ref 4	1	30 + 1	200	No
ref 5	1	60 + 1	150	No

The number of cells along r is always bigger than a multiple of 30 by 1 unit because we always add 1 extra cell to be treated separately in PHOENICS. This cell is made larger by employing a *null object* to ensure $y^+ > 30$. To be specific, the last cell goes from $r = 0.0475$ to the wall for all refinement levels.

All the meshes are based on cylindrical-polar coordinates. These mesh patterns were of interest to our analysis because we wanted to test the hypothesis that increasing the mesh refinement level along the axial coordinate wouldn't have caused a significant shift in the simulation results, indeed this was the case. Increasing the refinement level along the r direction was more problematic because it would lead the simulation closer and closer to the wall and, particularly when the power-law was enabled, it could stretch out the cells too much and create numerical instabilities, furthermore it could cause y^+ to be smaller than 30. This was ultimately solved by disabling the power law and by forcing the near-wall cells to be fixed in size. The chosen grid was the base one since it was computationally cheap while being fine enough to prove the test variables grid independent.

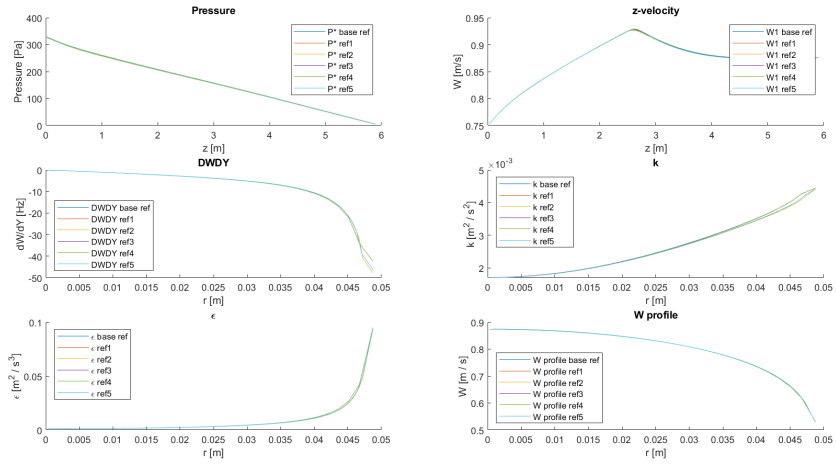

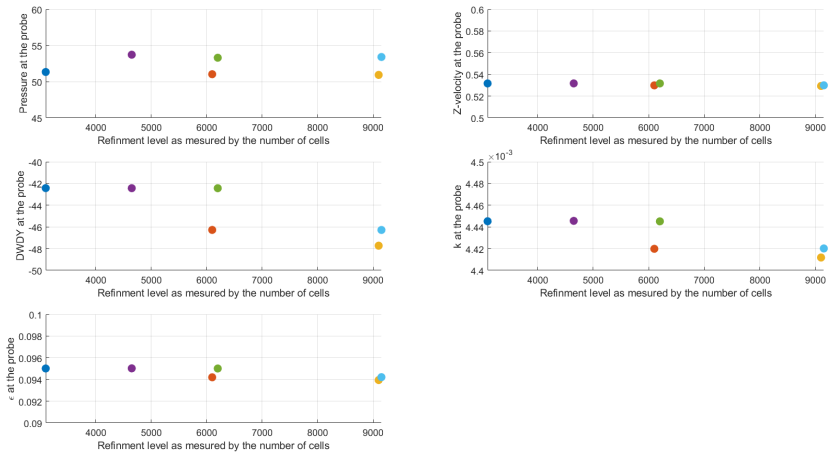

An arbitrary, quantitative criterion was formulated to more strongly support the claim of grid independence. After having linearly interpolated the values of W, $\frac{dW}{dy}$, P, k and ϵ on their respective storage points on the coarser meshes, we computed a **pseudo-L_1 norm** of the differences among the versions of these variables on various levels of grid refinement. This was done by calculating the sum of the absolute values of the point-wise differences of the variables being compared and then normalizing this sum by the number of cells in the coarser mesh. Note that the interpolation was done with respect to z in the computation of L_1 norms for P and W, with respect to r in the computation of the L_1 norms for $\frac{dW}{dy}$, k and ϵ. Some of the norms are reported below, they show that the most sensible variable is P^* but it too remains within acceptable values. Once again these results, even if they follow from a somewhat arbitrary definition of a norm, boost the solidity of our approach and prove once more that our findings are grid-independent.

Meshes	variable	L_1 norm
base vs **ref1**	P^*	0.89959
base vs **ref2**	P^*	1.1857
base vs **ref3**	P^*	0.77642
base vs **ref4**	P^*	1.1584
base vs **ref5**	P^*	0.42669
base vs **ref1**	dW/dy	0.20341
base vs **ref2**	dW/dy	0.34328
base vs **ref3**	dW/dy	0.005189
base vs **ref4**	dW/dy	0.0080483
base vs **ref5**	dW/dy	0.20758
base vs **ref1**	ϵ	0.00020381
base vs **ref2**	ϵ	0.00032258
base vs **ref3**	ϵ	4.275e-06
base vs **ref4**	ϵ	1.0779e-05
base vs **ref5**	ϵ	0.00020695

Meshes	variable	L_1 norm
base vs **ref1**	W	0.00054393
base vs **ref2**	W	0.00071945
base vs **ref3**	W	0.0002163
base vs **ref4**	W	0.00030179
base vs **ref5**	W	0.00066365
base vs **ref1**	k	2.7774e-05
base vs **ref2**	k	3.6314e-05
base vs **ref3**	k	1.5353e-06
base vs **ref4**	k	5.2722e-06
base vs **ref5**	k	2.8661e-05

5. Since no analytical solution is available for this case, the CFD results are compared against experimental data and empirical formulas available in the literature. Specifically, the experimental data originate from the PhD thesis by Lars Even Torbergsen (1998), who investigated the fully developed pipe flow of air at similar Reynolds number to those of the present test case. Our scope is to check that a proper selection of the modeling settings (here, the turbulence model) has been made, this process is called *validation*.

- Firstly, the validation is carried out by referring to the frictional losses, which are quantified through the friction coefficient f. Note that the friction coefficient, the skin friction coefficient C_f, the hydraulic gradient J, the pressure gradient $-\frac{dP^*}{dz}$ and the wall shear stress τ_w are interchangeable parameters related to the frictional losses. Thus, a validation with respect to say f is practically equivalent to a validation with respect to the others. The friction factor obtained from the CFD simulation is compared against the value obtained experimentally by Torbergsen, the Moody chart and the two formulas for hydraulically smooth pipes by Prandtl and by Haaland found below. The variability of these estimates is to be regarded as the inherent uncertainty in the evaluation of the friction factor. This means that we're not worried about not having a perfect match.

$$\frac{1}{\sqrt{f}} = -2log_{10}\left(\frac{2.51}{Re_b \cdot \sqrt{f}}\right) \tag{2}$$

$$\frac{1}{\sqrt{f}} = -1.8log_{10}\left(\frac{6.9}{Re_b}\right) \tag{3}$$

  The simulated f is obtained by first extracting τ_w from STRS, then $f = 4C_f = \frac{8*\tau_w}{\rho \cdot W_b^2}$ is a well-known consequence of the Darcy-Weisbach formula. A numerical solution for the formula by Prandtl is found by means of the *fzero* function in *MATLAB*.

- Secondly, the validation is carried out by referring to the Reynolds averaged axial velocity profile. For this variable, the terms of comparison include the data obtained experimentally by Torbergsen and presented in dimensionless form as $\frac{W}{W_b}$ versus $\frac{r}{R}$. Specifically, two data series are provided, which correspond to two different post-processing operations on the experimental data. We also compare against the power law profile of Nikuradse $W = W_b \frac{(2n+1)(n+1)}{2n^2} \cdot (1 - \frac{r}{R})^{\frac{1}{n}}$ where $n = f^{-0.5}$. In order to evaluate f, all its previous estimates shall be used, thus, the comparison will be made against three different literature curves. Finally we compare against the wall function of Launder and Spalding (in its range of validity) expressed in dimensionless form as w^+ versus y^+, i.e. $w^+ = y^+$ if $y^+ < 11.6$ and $w^+ = \frac{1}{k} \cdot ln(E \cdot y^+)$ if $11.6 < y^+ \leq 130$ where $k = 0.41$ is the Von Karman constant and E is a roughness coefficient set equal to 8.6 for hydraulically smooth walls. This comparison is made in it's own log-log plot.

- The validation is extended to the profile of the turbulent kinetic energy along the pipe radius. We present the results in dimensionless form as $\frac{k}{W_b^2}$ versus $\frac{r}{R}$ and compare against the data obtained experimentally by Torbergsen and the following empirical formula reported in the PhD thesis of Kam Hong Ng (1971). Once again all the estimates of f are used.

$$\frac{k}{W_b^2} = \frac{f}{8} \cdot \left[1 + \frac{2}{3}\left(\frac{r}{R}\right) + \frac{10}{3}\left(\frac{r}{R}\right)^3\right] \tag{4}$$

- Finally, the validation is focused on the profile of the turbulent dissipation rate. We present the results in dimensionless form as $\frac{\epsilon \cdot R}{W_b^3}$ versus $\frac{r}{R}$ and compare against the data obtained experimentally by Torbergsen. Specifically, three data series are provided, which correspond to different methods for estimating ϵ form the same experimental data point. The difference between the three series underlines the challenges in providing experimental estimates of ϵ. We also compare against the following relation at the basis of the standard k-ϵ turbulence model:

$$\epsilon(r) = C_d \frac{k^{\frac{3}{2}}(r)}{l_m(r)} \tag{5}$$

  where $C_d = 0.1643$, l_m is the mixing length, that is, a characteristic length scale of turbulence. In order to apply the formula here above, one must know the radial profiles of k and l_m, these are obtained respectively from the cubic correlation by Kam Hong Ng presented previously and from the following empirical distribution of Nikuradse.

$$l_m = R \cdot \left[0 - 14 - 0.08\left(\frac{r}{R}\right)^2 - 0.06\left(\frac{r}{R}\right)^4\right] \tag{6}$$

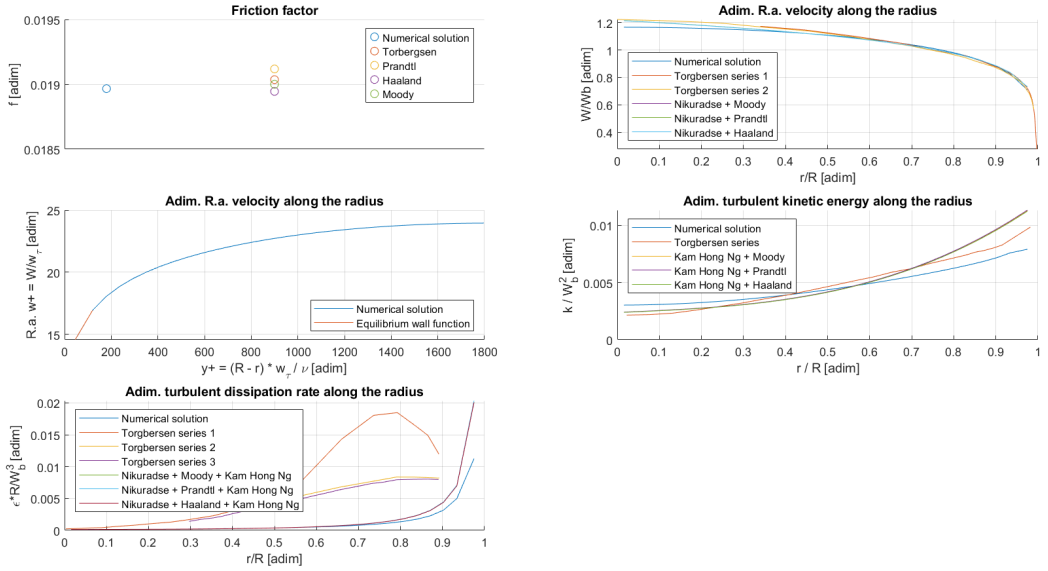

We observe a beautiful accordance of every variable in every plot except for ϵ, in that case the numerical solution agrees with the profile obtained by mixing literature formulas for every possible choice of f, but only faintly resembles the experimental series by Torbergsen. We consider this as a sign of the difficult-to-interpret and difficult-to-measure nature of ϵ, coupled with the fact that the experimental setup by Torbergsen resembles ours only in Reynolds number and not in viscosity or density, rather than as a sign of poor simulation quality.

6. The wall function approach employed in this test case requires the near wall cells to be characterized by y^+ above 30 and below 130. We run the numerical simulations disregarding this constraint, that is, we calculate the CFD solution on fine, near-wall meshes in order to analyze what happens when y^+ is outside the admissible range by referring to the friction factor, the Reynolds-averaged axial velocity profile, and the radial profiles of the turbulent variables k and ϵ. To achieve this the region from $r = 0.0475$ to the wall was divided into 15 cells for a first simulation, inducing $y^+ \approx 4$, and 40 cells for the second one, inducing $y^+ \approx 1.5$.

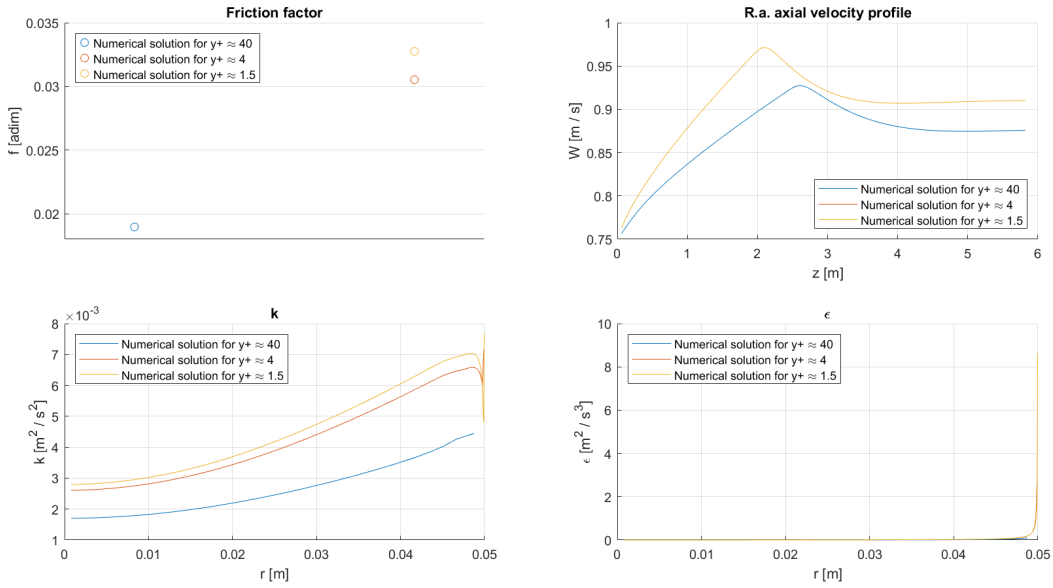

We observe a significant shift of the friction factor and of the axial velocity profile, as well as the signs of numerical instabilities in the plots of k and ϵ.

7. As an alternative to the wall function approach, the low-Reynolds one relies on the solution of the near-wall flow field up to the viscous sub-layer. This requires, on the one hand, defining very fine meshes close to the wall, so that the near-wall cells are characterized by $y^+ \approx 1$ and, on the other hand, modifying the turbulence model equations close to the wall by means of dumping functions. We solve the same test case using a low-Reynolds turbulence model, specifically, the Two-Layer k-ϵ model by Rodi (1991).

   Firstly, we verify that the simulation has converged by comparing the values of significant variables, such as f, after having stopped it at 15000 and at 30000 iterations: we get $f = 0.020472$ in both cases, demonstrating convergence. We repeat the analysis and validation steps also for this new turbulence model, this time our custom entry length criterion yields $L_e = 3.78$.

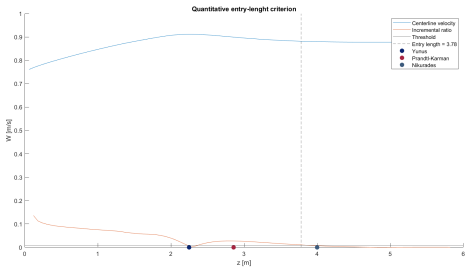

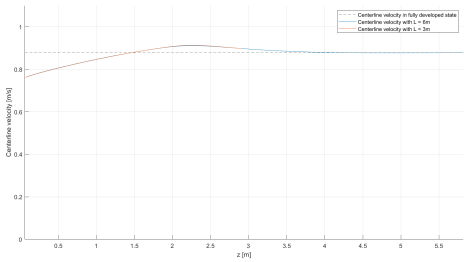

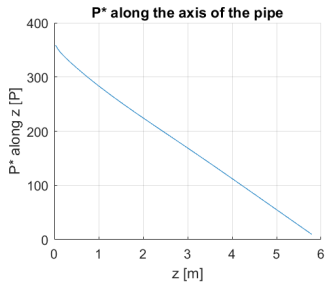

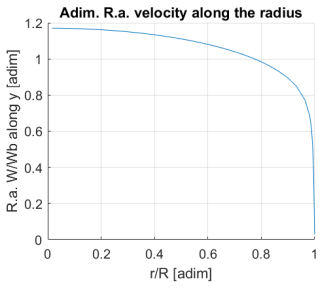

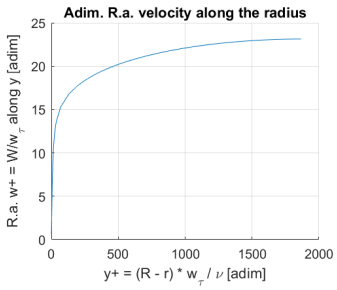

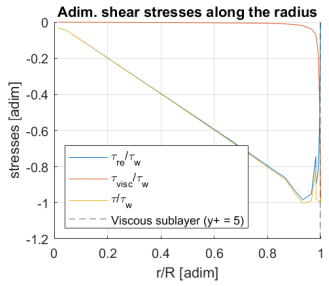

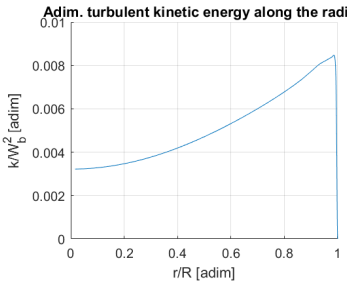

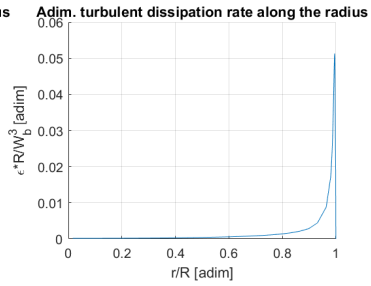

The grid independence study requires defining a set of new meshes the details of which can be found below, once again we end up choosing the base mesh.

Mesh name	# cells along x	# cells along y	# cells along z	Power law
Base case	1	30 + 30	100	No
ref 1	1	60 + 30	100	No
ref 2	1	90 + 30	100	No
ref 3	1	30 + 30	150	No
ref 4	1	30 + 30	200	No
ref 5	1	60 + 30	150	No

The region from $r = 0.0475$ to the wall is divided into 30 cells for all refinement levels to ensure $y^+ \approx 1$.

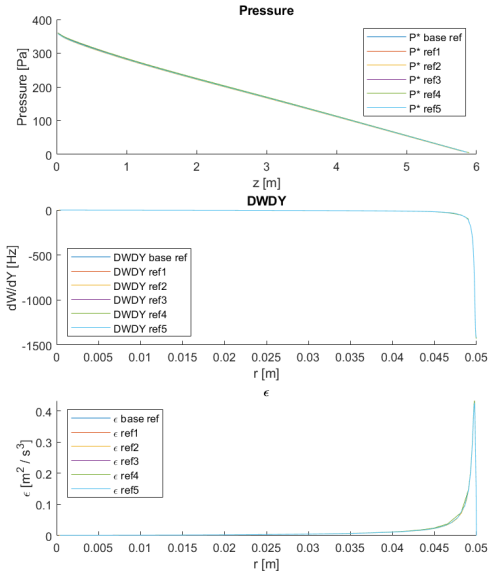

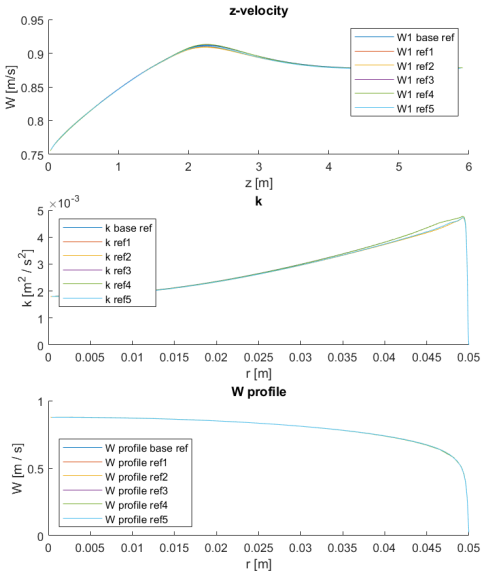

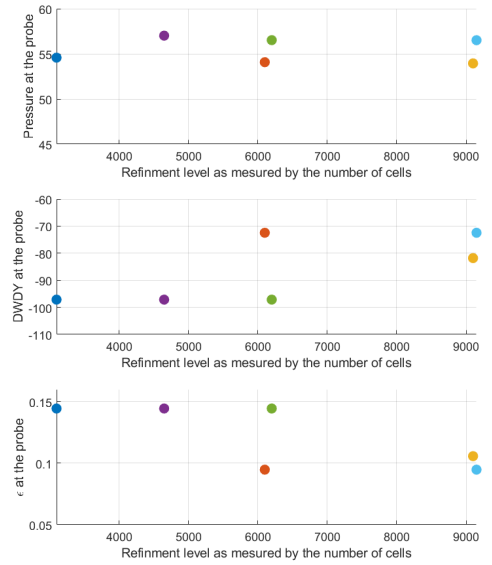

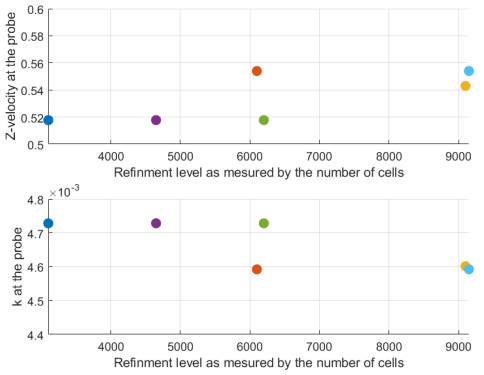

Meshes	variable	L_1 norm
base vs **ref1**	P^*	1.3222
base vs **ref2**	P^*	1.658
base vs **ref3**	P^*	0.65553
base vs **ref4**	P^*	1.0008
base vs **ref5**	P^*	0.7904
base vs **ref1**	dW/dy	1.4324
base vs **ref2**	dW/dy	1.8086
base vs **ref3**	dW/dy	0.012998
base vs **ref4**	dW/dy	0.012468
base vs **ref5**	dW/dy	1.4225
base vs **ref1**	ϵ	0.0022328
base vs **ref2**	ϵ	0.0027389
base vs **ref3**	ϵ	1.6406e-05
base vs **ref4**	ϵ	1.5467e-05
base vs **ref5**	ϵ	0.0022201

Meshes	variable	L_1 norm
base vs **ref1**	W	0.00081371
base vs **ref2**	W	0.0010358
base vs **ref3**	W	0.00026582
base vs **ref4**	W	0.00040711
base vs **ref5**	W	0.00079445
base vs **ref1**	k	4.1283e-05
base vs **ref2**	k	5.0275e-05
base vs **ref3**	k	6.9923e-07
base vs **ref4**	k	1.8198e-06
base vs **ref5**	k	4.1663e-05

Since with this approach we are solving much smaller scales than what we did with the wall function approach which modeled them, better accuracy is to be expected close to the walls but that comes with increased computational complexity. It also proved more difficult to make this kind of simulation converge as the residuals oscillated more than with the wall-function approach and the pseudo L_1 norms are slightly higher too. Among these new plots, it is particularly interesting to observe the shear stress profile and its components: while it's true that some numerical instability seems to have hindered the simulation at about $\frac{r}{R} = 0.9$, the overall trend of the stresses better matches the theorical one with respect to the previous simulations. Another interesting plot is that of ϵ: now it's possible to see the sudden drop that takes place very close to the walls and that was previously hidden.